Pulsed Force Kelvin Probe Force Microscopy

Devon S. Jakob¹, Haomin Wang, ¹ and Xiaoji G. Xu¹

¹Department of Chemistry, Lehigh University, 6 E Packer Ave. Bethlehem, PA, 18015, United States

Corresponding Email: xgx214@lehigh.edu

Abstract

Measurement of the contact potential difference (CPD) and work functions of materials are important in analyzing their electronic structures and surface residual charges. Kelvin Probe Force Microscopy (KPFM), an imaging technique of atomic force microscopy, has been widely used for surface potential and work function mapping at the nanoscale. However, the conventional KPFM variants are often limited in their spatial resolution to $30 \sim 100$ nm under ambient conditions. The continuingly decreasing size and increasing complexity of photoactive materials and semiconductor devices will present future challenges in uncovering their nanometer-scale electrical properties through KPFM. Here, we introduce a KPFM technique based on the pulsed force mode of atomic force microscopy. Our technique, named pulsed force Kelvin Probe Force Microscopy (PF-KPFM), is a single-pass technique that utilizes the intrinsic Fermi level alignment between the AFM tip and the conductive sample without the need for external oscillating voltage. Induced cantilever oscillations generated by a spontaneous transfer of electron redistribution between tip and sample are extracted and used to obtain the cantilever oscillation amplitude and to derive the surface potential. The spatial resolution of PF-KPFM is shown to be <10 nm under ambient conditions. The high spatial resolution mapping of surface potential enables in situ determination of ohmic and non-ohmic contact between metals and semiconductors, mapping boundaries of ferroelectric domains of BaTiO₃, as well as characterization of protein aggregates. High spatial resolution measurements with PF-KPFM will facilitate further studies directed at uncovering electrical properties for emerging photoactive materials, biological samples, and semiconductor devices.

Keywords

Kelvin probe force microscopy, contact potential, work function, atomic force microscopy, photovoltaics, semiconductor devices, peak force tapping

When in contact, two dissimilar metals or semiconductor materials generate a contact potential. In Kelvin probe method, the contact potential difference (CPD) between a metal and a reference electrode is defined as

$$CPD = \frac{\phi_S - \phi_R}{e} \tag{1}$$

where e is the unit electrical charge, and ϕ_S and ϕ_R are the work functions of the sample and reference metals, respectively.² The work function is intrinsically connected with the Fermi level of the material and is closely related to the electrical and optical properties of the materials.³⁻⁶ Kelvin probe force microscopy (KPFM) is an imaging technique based on atomic force microscopy (AFM) that utilizes the proximity of a metal-coated AFM probe with a conductive or semi-conductive sample to measure the relative contact potential difference. For insulator samples, KPFM reveals residual charges that are locally bound to the surface of the sample. KPFM is a robust and popular tool and has been applied to a wide range of samples for surface electrical characterizations, including functional optical films,⁷ semiconductor devices,⁸ ferroelectrics,⁹ perovskites,¹⁰ optically-active biological molecules,¹¹ and metallic nanostructures.¹²

Traditionally, there are two main types of KPFM: amplitude-modulation Kelvin probe force microscopy (AM-KPFM) and frequency-modulation Kelvin probe force microscopy (FM-KPFM). Both types operate in the tapping mode of AFM and rely on external charging of the AFM probe with an oscillating (AC) voltage. In AM-KPFM, the probe is driven at its mechanical resonant frequency at a defined distance above the sample. The AC voltage applied between the tip and the sample leads to an electrostatic force (*i.e.*, Coulomb force) that causes additional induced oscillations in the AFM cantilever at the AC frequency. A superimposed DC offset voltage is applied between the probe and sample to nullify the induced oscillations, resulting in a measurement of the CPD. ¹³ FM-KPFM measures the gradient of the electrostatic force, rather than the amplitude of the induced oscillations. The electrostatic force gradient changes the mechanical resonant frequency of the AFM probe, resulting in an oscillation phase shift. The phase shift is nullified with a superimposed DC offset voltage, again resulting in the CPD measurement. ¹⁴

It is most convenient to measure the majority of samples and materials in ambient conditions. For these measurements, AM- and FM-KPFM have intrinsic limitations. External charging of the AFM probe with a large AC voltage, typically several volts, is required and may result in unwanted electrochemical reactions. A momentary contact between the probe and sample may result from imperfect AFM feedback or from abrupt changes in surface topography, which result in electrochemical damage and image artifacts as electrons transfer between tip and sample at several volts of AC voltage. To avoid sample damage and image artifacts from imperfect feedback, a lift mode (*i.e.*, second pass scan) is used. In the lift mode, the AFM first scans the topography of the sample with a simple scan under the AFM feedback, *e.g.*, tapping mode. Then, the AFM probe is lifted to a certain height to acquire the CPD measurement, following the trajectory acquired during the topography scan, without AFM feedback. The need for a second pass in lift mode results in additional time requirements. Also, because the second pass is not under the AFM feedback, the lift height must be large enough to withstand external instrument vibrations and thermal drift that may lead to tip crashing into the sample surface.

The low spatial resolution of current KPFMs under ambient conditions is limited by the long-range nature of the Coulomb force. The Coulomb force is not isolated to only the tip apex, as it also interacts with the tip cone and the cantilever shaft. The resulting CPD measurement is an average of all of these electrostatic contributions. ¹⁵ Given the fact that the tip cone and cantilever shaft are far larger than the tip apex, the stray capacitance from each results in large background Coulomb forces during CPD measurement, reducing the spatial resolution. Moreover, the background contribution from the tip cone and cantilever shaft to the Coulomb force increases with the increase of the tip-sample distance. 16 The spatial resolutions of KPFMs that use lift mode are worsened by the necessity for large tip-sample distances during CPD measurement. Consequently, AM-KPFM gives a spatial resolution of ~100 nm; FM-KPFM gives about 30~50 nm spatial resolution under ambient conditions. Significant improvement of the spatial resolution can be achieved when operating in ultra-high vacuum (UHV) and low-temperature conditions, where the mechanical noise and the thermal drift are significantly reduced—enabling a very low lift height and a low AC voltage requirement. The increased Q-factor of the cantilever in UHV also improves the KPFM signal, leading to the improvement of spatial resolution < 1 nm. 17, 18 However, maintaining UHV and low-temperature conditions adds significantly extra experimental complexity, cost, and measurement time. Also, the UHV condition is not suitable for measuring samples that are incompatible with vacuum conditions, such as biological samples or samples that have high vapor pressures.

To ensure that the KPFM technique remains a useful tool for analyzing emerging heterogeneous materials with nanoscale features, the next major innovation should consist of the following improvements:

- 1. avoid the need for large AC voltages between the tip and the sample;
- 2. concentrate the electrostatic contribution as much to the tip apex as possible;
- 3. avoid the lift mode or the second pass that is not under AFM feedback;
- 4. deliver an improved spatial resolution under the ambient conditions.

To address these needs, we have invented *Pulsed Force Kelvin Probe Force Microscopy* (*PF-KPFM*), which is based on a different measurement paradigm than the existing AM- and FM-KPFM techniques. Our technique generates and detects the Coulomb force between the tip and sample based on intrinsic Fermi-level alignment, bypassing the need for an external AC voltage. Our method is based on the pulsed force mode of AFM, ¹⁹ popularly known as the peak force tapping mode. ²⁰ We show that PF-KPFM can map the CPD with < 10 nm spatial resolution under the ambient conditions without the lift mode on a wide range of samples.

Results and Discussion

Detection of the Coulomb Force Induced by CPD in Pulsed Force Mode

When the metallic AFM tip and the sample are detached during the PFT cycle, they form a nanoscale capacitor with capacitance C that is determined by the geometry of the tip and the sample. The electrical potential energy U of the capacitor is described by Equation (2):

$$U = \frac{1}{2}CV^2 \tag{2}$$

in which V is the voltage between the AFM tip and the sample underneath. V is determined by the CPD and the external bias voltage V_{DC} with a relation $V = V_{DC} - V_{CPD}$. The Coulomb force along the vertical direction between the tip and sample can be derived by differentiating the electrical potential energy U with respect to the Cartesian coordinate z perpendicular to the sample surface in Equation (3):²

$$F = -\frac{\partial U}{\partial z} = -\frac{1}{2} \frac{\partial C}{\partial z} (V_{DC} - V_{CPD})^2$$
 (3)

Without an external bias voltage ($V_{DC} = 0$), the Fermi level alignment causes a voltage that equals the CPD to form between the tip and the sample. As a result, an induced Coulomb force $F = -\frac{1}{2}\frac{\partial C}{\partial z}V_{CPD}^2$ emerges when the tip and sample are electrically connected. In our method, we implement a field-effect transistor (FET) between the tip and sample to mediate the electrical connection. The schematic of PF-KPFM is shown in **Fig. 1a** and detailed in the *Methods* section. As soon as the FET is switched ON, spatially separated charges form between the tip and sample, resulting in a Coulomb force. The induced Coulomb force leads to free-space cantilever oscillations, which are later damped when the tip and sample come into contact during every peak force tapping (PFT) cycle.

The cantilever oscillations due to the induced Coulomb force without external bias voltage are shown in detail in Fig. 1b. The cantilever deflection after tip-sample detachment is shown as the red curve and the pulse train of voltage to the FET is shown as the blue curve. When the FET connection state is switched ON, the FET acts as a conducting wire, allowing electrons to move between the metallic tip and the sample to achieve Fermi level alignment. The charges between the tip and the sample exert Coulomb force described by Equation (3). When the FET connection state is OFF, the FET acts as a capacitor and the electrical connection between tip and sample is severed. The existing charges between the tip and the sample redistribute between the tip-sample capacitor and the residual capacitance of the FET. The FET (J109, Fairchild) has a residual capacitance of 0.6 to 0.8 nF when it is switched OFF. In comparision, the capacitance of the tipsample configuration is on the order of 10^{-17} F. The residual capacitance of the FET during the OFF state is far larger than the tip-sample capcacitor when the tip is retracted several nanometers from the sample surface. Therefore, the charges that are generated due to Fermi-level alignment when the FET is switched ON migrate to the source/drain junction of the FET when it is switched OFF, leading to a strong reduction of the Coulomb force between the tip and sample. Therefore, periodically switching FET connection states between ON and OFF will cause periodical force on the cantilever to induce oscillations. The induced cantilever oscillations persist until the next tipsample contact if a cantilever with high quality factor is used, which is shown in Fig 1b. By performing a fast-Fourier transform, the oscillations can be processed into the frequency domain. A characteristic peak at the cantilever free-space resonance emerges (shown in Fig. 1d). The total amplitude of the resonant peak in the frequency domain is integrated to be used as a measure of the Coulomb force, or for CPD measurement as described in the next section. Once the tip and the sample are in physical contact, the charges that are stored inside the residual capacitance of the

FET are recombined and neutralized, restoring the system for the next event of Fermi-level alignment in the next peak force tapping cycle.

Mapping of Induced Cantilever Oscillation by Coulomb Force

The mapping of induced Coulomb force is achieved by registration of the induced Coulomb force while the AFM tip is spatially scanned over the sample. Figure 2 shows the measurement of the induced cantilever oscillation by Coulomb force on a standard KPFM calibration sample (PFKPFM-SMPL, Bruker). This sample consists of gold (Au) and aluminum (Al) islands on a silicon (Si) substrate. The work function differences between these three regions and the platinum AFM tip are well known, allowing it to be used as a benchmark sample for PF-KPFM. Fig. 2a shows the topography of the sample. Fig. 2b displays the Coulomb-force induced cantilever oscillation acquired by PF-KPFM. The induced cantilever oscillation on the Al area is greatest among the three regions, meaning Al induces a greater Coulomb force than Si or Au. On the other hand, Au produces the weakest Coulomb force, as the oscillation amplitude is smallest on this region. This observation can be understood by considering the differences in work functions. During Fermi-level alignment, a greater work function difference requires more electrons to migrate, thus resulting in a higher density of separated charges between the tip and sample. In our experiment, we use a platinum tip $(\phi_{Pt} = 5.12 - 5.93 \text{ eV})^{21}$ Since the work function of Al $(\phi_{Al} =$ 4.06 – 4.26 eV)is the furthermost from that of platinum, the induced Coulomb force signal for Al is the highest.²¹ On the other hand, since the work function of Au ($\phi_{Au} = 5.10 - 5.47$ eV) is only slightly lower than the work function of platinum a small Coulomb force is observed.²¹ The Coulomb force induced cantilever oscillation amplitude from a zoomed-in region between the Si and the Au region (white dashed box in Fig. 2b) is shown in Fig. 2c for detail. A cross section along the Si/Au boundary is shown in Fig. 2d to estimate the spatial resolution. A drastic spatial change of the Coulomb force induced oscillation amplitude is observed across 7 nm, suggesting the high spatial resolution read-out of cantilever oscillation from induced the Coulomb force. This high spatial resolution measurement of Coulomb force suggests that the Coulomb force is primarily localized to the tip apex, and furthermore holds the key to high spatial resolution surface potential imaging.

Determination of CPD through the Measurement of Coulomb Force Induced Cantilever Oscillation Amplitude

According to Equation (3), when the external DC bias voltage equals CPD ($V_{DC} = CPD$), the Coulomb force between tip and sample is negated and the induced oscillations are removed. Therefore, by sweeping the external DC bias voltage on the sample, we can accurately obtain the CPD at individual locations from values of V_{DC} which minimize the induced cantilever oscillation. **Figure 3** displays the measured oscillation amplitude *versus* V_{DC} on the Au, Si, and Al areas of the calibration sample. **Fig. 3a** shows the topography of the sample. The locations of measurement are marked by the black, blue, and red dots on Al, Si, and Au respectively. **Fig. 3b** displays the cantilever oscillation amplitude *versus* V_{DC} relationships on the three corresponding locations. Three V-shaped curves are observed. The intersections of the two branches of each V-shaped curve are located at different V_{DC} locations for each substrate. These intersections reveal the corresponding surface potential values between the sample and the Pt-coated AFM tip. The

measurement provides an accurate CPD between Al and Pt to be -973 ± 3 mV, the CPD between Si and Pt to be -404 ± 3 mV, and the CPD between Au and Pt to be -127 ± 3 mV. The error is calculated from least squares fits on each of the V-shaped curves, while its small magnitude suggests that accurate values of CPD can be found through DC bias sweeping. This level of precision is comparable to that of AM-KPFM, and is much better than the FM-KPFM.²²

The phase of the cantilever oscillation can also be used to measure the CPD. The oscillation phase is the phase difference between the mechanical oscillation phase and the electrical waveform that drives the periodical switching of FET on the electrical connectivity. **Fig. 3c** shows the corresponding phase of the cantilever oscillations at the three locations. The CPD value corresponds to the condition where the oscillation phase equals $\pi/2$. The cantilever oscillation phases can be utilized to identify the DC bias voltage corresponds to which branch of the V-shape response, which is utilized for feedback during surface potential mapping. The oscillation flips phase from close to zero to close to π when the DC bias voltage V_{DC} corresponds to different branches. The change in the cantilever deflection that results from phase shifting is shown in **Supplementary Figure S1**.

Mapping of Surface Potential with Negative Feedback Loop in PF-KPFM

In PF-KPFM, the surface potential is continuously mapped while the tip is scanned over the sample in pulsed force mode. To obtain the surface potential, the cantilever oscillation amplitude is used as a process variable within a negative feedback loop. The feedback loop controls the DC bias voltage V_{DC} that is applied between the AFM tip and the sample, so that the induced cantilever oscillations maintain a setpoint \mathbf{s} . The operation mechanism of the feedback loop is illustrated in **Figure 4** and explained in detail in the *Methods* section. The feedback loop operates simultaneously with the AFM scans, providing the DC compensation voltage V_{DC} at every spatial location to form the KPFM image. For simplicity, the KPFM images herein are presented in terms of surface potential, which is given as -CPD, which is the negative value of the contact potential difference.

In the ideal case, the external setpoint s is set to be zero, so that $V_{DC} = CPD$. In practice, we have found that if the value of the setpoint s is too small, it reduces the performance of the feedback loop. Therefore, we choose the setpoint s to be a small value for the induced cantilever oscillation under the control of the feedback loop. However, since the cantilever oscillation amplitude exhibits a V-shaped behavior, *i.e.*, for a given oscillation amplitude, there are two corresponding V_{DC} values (illustrated in the dashed inset of **Fig. 4**). Such ambiguity creates a problem for the feedback: if there were abrupt spatial changes of the sample work functions, the feedback could be perturbed to switch branches of the V shape, leading to a jump in the compensation values. To solve this problem, we use both the amplitude and the phase of the cantilever induced oscillations in the feedback loop. As **Fig. 3c** illustrates when the V_{DC} switches branch, the oscillation phase will jump across $\frac{\pi}{2}$. By tracking the phase of the cantilever oscillation, the feedback mechanism can identify if switching of branches occurs. A sudden jump of phase across $\pi/2$ is used to identify the crossing of the branches in the feedback loop and is used to help

the system to restore proper feedback conditions. Thus, the feedback loop can reliably operate at a small set point near the CPD without ambiguity.

Operating the feedback loop at a small non-zero set point leads to a value of V_{DC} slightly offset from the CPD. The small offset can be compensated using the following equation:

$$CPD = V_{DC} - \frac{s}{k} \tag{4}$$

where k is the slope of one of the two branches of the oscillation amplitude *versus* bias voltage. The slope can be obtained from linearly fitting one of the two branches of oscillation amplitude *versus* DC bias sweep, such as shown in Fig. 3b. V_{DC} is the DC bias compensation value from the negative feedback loop which causes the cantilever oscillation amplitude to matches the setpoint s.

Figure 5 shows the surface potential mapping over the same sample area previously presented in Figure 2. The topography is shown in Fig. 5a. The surface potential values of the Au, Si, and Al areas, shown in Fig. 5b are clearly revealed by PF-KPFM. The value of $\frac{s}{k}$ for this measurement is 502 ± 21 mV, and is accounted for in the surface potential maps. Since the error here is derived from linear regression, it is highly influenced on the choice of setpoint; lower setpoints will achieve lower error at a cost of the spatial resolution of the image as the PID loop used in the setup becomes less responsive. A zoomed-in region of the boundary between Si and Au is imaged and shown in Fig. 5c for detail. A sectional profile across the boundary (marked by the red line in Fig. 5c) is obtained and displayed in Fig. 5d. From the profile, an estimated spatial resolution of 10 nm is obtained, which is superior to the spatial resolution of the FM-KPFM under ambient conditions. A comparison of the same area obtained from FM-KPFM while using the same type of platinum-coated probe is included in Supplementary Figure S2.

Revealing Junction Type at Semiconductor/Metal Boundary

One interesting observation in the surface potential map in **Figure 5** is the difference between the Al/Si boundary and the Si/Au boundary. The Al/Si boundary in the surface potential map appears to be gradual and continuous, whereas the Si/Au boundary in the surface potential map is sharp and well defined. **Figure 6** displays the zoomed-in region of these two boundaries. **Fig. 6a** is the topography of an Al/Si boundary. **Fig. 6b** is the CPD map of the Al/Si boundary. **Fig. 6c** shows the topography of a Si/Au boundary. **Fig. 6d** shows the CPD map of the Si/Au boundary. The sectional profiles of the surface potential and the topography are displayed in **Fig. 6e**. The surface potential values across boundaries are represented by the red curve. The topography of the sample is represented by the blue curve as a reference to locate the boundaries.

Fig. 6f schematically illustrates the relative band positions of the three metals within the calibration sample together with the measured surface potential from **Fig. 6e**. The Fermi levels of the three metals with respect to each other are shown to exist before electric contact, since the Fermi levels are assumed to be equal to each other after the metals are deposited onto the Si. The relative positions of the Fermi levels also indicate the direction of electron flow within the sample, with electrons migrating from high to low Fermi levels. The bending of the surface potential near the Al/Si boundary reveals the behavior of interfacial electrons after contact. The surface potential

at the Al/Si boundary exhibits a downward bending on the Al side, indicating an Ohmic contact. Since the Fermi level is assummed to be aligned and at thermal equilibrium, the decreasing Fermi level energy indicates that the vacuum level energy decreases over this distance. In contrast, the boundary between Si/Au does not exhibit long-range bending in the surface potential measurement, suggesting that the energy of the vacuum level changes rapidly at the interface of Si/Au. The difference in behaviors could be understood as following. The Al/Si sample consists of a thin film of Al deposited on the Si substrate, allowing for a thin spatial charged layer that exists vertically between Al and Si. The gradual lateral variation of surface potential on the Al side is due to the presence of Si on its right side that serves as a pertubation to the vertical spatial charged layer of Al and Si, breaking the translational symmetry. Because of the ohmic contact between Al and Si, the perturbation is not blocked. On the other hand, the interface between Si/Au shows much more well-defined surface potential that rapidly changes near the interface, indicating a non-Ohmic contact, where a barrier formed to prevent electron migrations. The Si in this experiment is p-doped, indicated by the small measured surface potential of ~300 mV between Si and Au in Fig. 6e.²³ A Schottky junction exists between Si/Au with an energy barrier preventing electrons from freely migrating. Instead, electrons in Si migrate toward the interface with Au, increasing the surface potential at the interface on the Si side. As a result, a small space-charge layer is formed on the Au side near the interface to balance the electrons at the Si side, which decreases the surface potential (increases the work function) on the Au side. Fig. 6f schematically illustrates the local accumulation of charges between Al/Si and Si/Au boundary.

The high spatial resolution of PF-KPFM at ~ 10 nm reveals the difference of ohmic contact *versus* non-ohmic through revealing the formation of space-charge layers. If regular, low-spatial resolution KPFMs were used, the sharp surface potential difference of non-ohmic contact would be smeared out and become hardly distinguishable with the ohmic contact. Direct identification of the types of contact through surface potential mapping would be difficult for regular KPFMs.

Enhancement of Signal Read-Out through Periodic FET Switching

In PF-KPFM, we implement a waveform consisting of multiple transistor-transistor logic (TTL) voltages to switch the FET states during every peak force tapping cycle. The temporal spacing of the TTL voltage waveform matches that of the free-space cantilever resonant oscillation. Therefore, the induced cantilever oscillations by the Coulomb force are coherently amplified. The concept is similar to the multiple excitations used in peak force infrared microscopy.²⁴ The increased signal magnitude improves the signal quality, and also increases the spatial resolution, as it enables a faster feedback response. **Figure 7** illustrates the comparison between several FET switching regimes on a MAPbBr₃ perovskite sample. **Fig. 7a**, shows the flat MAPbBr₃ region together with bumpy areas, which are likely generated from degradation. A comparison of the induced cantilever oscillations under 1-pulse, 3-pulse, and 5-pulse FET switching are displayed in **Fig. 7b**. The oscillation amplitude increases as the number of electrical connections are increased, yielding an improvement in signal strength and sigal to noise ratio. The improvement in the SNR is evident in the surface potential map shown in **Figs. 7c-d**, where high SNR improves the performance of the feedback loop with improved spatial resolution. More details of the surface potential variations are revealed in 5-pulse PF-KPFM than 1-pulse PF-

KPFM. Note that the surface potential values do not change as a function of the number of FET pulses. Instead, the slope k of the branch on which feedback is operating on changes, leading to more efficient feedback.

Revealing Ferroelectric Boundaries of BaTiO₃

Below the Curie temperature, barium titanate (BaTiO₃) and other ferroelectric oxides are able to spontaneously polarize, forming anisotropic ferroelectric domains.²⁵ The presence of ferroelectric domains together with their ability to change direction under an applied electric field has led to their usage in memory storage devices²⁶, microelectromechanical actuators and sensors²⁷, medical ultrasound imaging devices²⁸, signal processing in optical communication systems²⁹, and photovoltaics.^{30, 31} Studies on the local ferroelectric domains of BaTiO₃ will help to improve the functionality of BaTiO₃. KPFM and piezo force microscopy have been previously implemented to study the local sample crystallographic orientation of anisotropic materials, since the surface potential of BaTiO₃ is strongly related to polarization-induced bound charges.^{9, 32, 33} However, information at the nanometer-scale is difficult to access, if the spatial resolution is insufficient. PF-KPFM is capable of imaging the surface potential of materials at the nanoscale with high spatial resolution. Fig. 8a shows the topography of a BaTiO₃ pellet, compressed from powders by a pellet press of 6×10³ psi. The variation of the surface potential over this area is revealed by PF-KPFM and shown in Fig. 8b. Because the sample consists of compressed powders, the ferroelectric domains are mostly localized to individual grains. Of particular interest is the location marked by the white box. This area consists of a single grain of high CPD which is packed in between grains of lower surface potential. To show that the surface potential is decoupled from the topography, two dotted lines are shown (marked (1) and (2)) over areas of low topography. The area marked (1) exhibits a lower surface potential than much of its surroundings, while the area marked (2) exhibits a much higher surface potential than its surroundings, even though both areas have low topography compared to their surroundings. Since the surface potential of BaTiO₃ is affected by the unit cell orientation, it should be possible to extract information on the orientation based on the PF-KPFM results. Fig. 8c shows a histogram created from the PF-KPFM image. Two prominent peaks are found, suggesting that the relative orientation of a majority of the polarization vectors are in two primary directions relative to each other. Surface potential values of 0.51 V and 1.04 V are extracted as the two averages, and they are similar to previously reported values from KPFM measurements on BaTiO₃.³³ A spatial resolution of 9 nm is extracted from the cross section indicated by a red line in Fig. 8b and is shown in Fig. 8d, demonstrating the high spatial resolution of PF-KPFM.

Multimodal Measurements on Protein

The maximum tip-sample interaction force is externally controlled in pulse force mode and can be made very small. The soft-contact regime allows for PF-KPFM to non-destructively image delicate samples such as biological materials. KPFM has been extensively used in the past to measure the electrical properties of soft biological samples; in particular, the label-free detection of biomolecules,³⁴ and the binding behavior of biomolecules.^{35,36} The high spatial resolution of PF-KPFM will be helpful in uncovering the heterogeneous charge dispersion that may be present in proteins and other biological materials at the nanoscale. In **Figure 9**, we show our results on

imaging bovine serum albumin (BSA) at the nanoscale, which was deposited on a Si substrate under neutral pH conditions by dropcasting. **Fig. 9a** shows the topography of the BSA structure. The topography map shows the presence of numerous oligomers dispersed throughout the surface of the substrate, which has been shown to occur in BSA under neutral conditions. ³⁷ Due to their small geometry, the electrical measurements of protein oligomers is difficult with conventional KPFM techniques. However, the surface potential of the protein and the protein oligomers is revealed by PF-KPFM in **Fig. 9b**. For further evaluation of the surface potential, a background-subtracted histogram is shown in **Fig. 9c** to show the heterogeneity of the surface potential for just the protein. The histogram reveals a double-Gaussian dispersion of the surface potential for the protein, with an overall average surface potential of 1.76 ± 0.06 V. Similarly, the surface potential for the protein oligomers is isolated and represented in a histogram in **Fig. 9d**. The surface potential values for the protein oligomers forms a Gaussian distribution with a center of 1.86 ± 0.09 V. Interestingly, the average contact potential for the protein is lower than the average contact potential for the surrounding protein oligomers, suggesting that the protein retains a higher positive charge at the surface in comparison to the oligomers.

The operational paradigm of PF-KPFM is different from existing KPFMs in terms of three aspects. First, PF-KPFM does not require the application of an external AC voltage to drive cantilever oscillations. Instead, switching of a low-resistance electrical connection between the tip and sample is implemented through a FET. Avoiding the application of large amplitude AC voltage means that related imaging artifacts and distortions are naturally absent in PF-KPFM. If tip-sample contact occurs when the FET is in the ON state, sample damage is unlikely to occur due to the absence of the AC driving voltage. Additionally, high voltages associated with traditional KPFMs could also result in bias-induced band bending, leading to inaccurate measurements of the surface potential, especially in the case of semiconductor samples.³⁸

Second, the PF-KPFM does not require the lift mode and does not suffer from electrical damage or imaging artifacts from the lack of the lift mode in traditional KPFMs. When the FET is in the ON state and the electrical connection is open, the tip and the sample are guaranteed to be detached in the peak force tapping cycle, in a configuration equivalent to the lift mode, but without the additional operational time of the second pass. Additionally, PF-KPFM is always operating under AFM feedback, unlike lift mode. In comparison, conventional KPFMs in tapping mode without the lift mode suffer from imaging artifacts even sample damages. This attribute is particularly meaningful for the measurement of delicate and unstable samples, such as the emerging perovskite photovoltaic materials and biological samples.

Thirdly, the generation of induced Coulomb force in PF-KPFM is specially designed to correspond to a tip-sample configuration when the tip-sample distance is very small, right after the tip-sample detachment in the peak force tapping cycle. Under the small tip-sample distance, the lightning rod effect concentrates the charges at the apex of the AFM tip, increasing the signal contribution from the apex region. ¹⁶ In contrast, tapping mode KPFMs under the ambient condition obtain signals from a large averaged tip-sample distances. The large tip-sample distance in regular KPFMs inevitably reduces the spatial resolution. As a result, the spatial resolution of PF-KPFM is

demonstrated to be ≤ 10 nm, in contrast to the typical 30 - 50 nm spatial resolution of FM-KPFM in ambient conditions.

Note that the pulsed force Kelvin probe force microscopy is fundamentally different from the current PeakForce KPFM[™] marketed by Bruker. PeakForce KPFM[™] is a dual-pass interleave method by using the regular peak force tapping mode for topography and tapping mode FM-KPFM in lift mode for CPD measurement. The performance and the spatial resolution of PeakForce KPFM are similar to that of a dual-pass FM-KPFM. Our PF-KPFM does not require the lift mode nor operates in the tapping mode. PF-KPFM is constructed by integrating the measurement of Kelvin probe force into the peak force cycle. It provides better spatial resolution and less measurement time than the PeakForce KPFM[™].

Conclusion

In conclusion, we have reported on a widely applicable KPFM technique that operates entirely in the pulsed force mode of AFM. PF-KPFM operates on a measurement paradigm based on the Coulomb force generated from intrinsic Fermi level differences, rather than from applying external AC voltage. The PF-KPFM is shown to provide a spatial resolution of <10 nm in surface potential imaging in ambient conditions, which surpass that of the FM-KPFM under similar conditions by at least three times. PF-KPFM overcomes many limitations of current KPFM techniques by bypassing the necessity for the lift mode scans or signal generation from stray capacitance. PF-KPFM is expected to enhance the applications of existing KPFMs with an improved spatial resolution that delivers more spatial details. PF-KPFM will facilitate the characterization of photovoltaics, semiconductor structures, as well as nano- to microscale biological samples with residual charges. PF-KPFM may also be used to reveal temporal dynamics of surface potential, enhancing the existing capabilities for time-resolved KPFM studies.^{39, 40} The operational principle of PF-KPFM is also compatible with other peak force tapping based technologies, such as the peak force infrared microscopy⁴¹ and the peak force scattering near-field optical microscopy⁴² for correlative chemical, near-field optical, electrical, and mechanical measurement.

Methods

The experimental apparatus of PF-KPFM is illustrated in **Fig. 1a**. The apparatus consists of the following components: an AFM with peak force tapping mode (equivalent to pulsed force mode) (Multimode 8 and Nanoscope V, Bruker); a lock-in amplifier with a built-in negative feedback loop (HF2LI with PID, Zurich Instruments); and a voltage-gated circuit controlled by a field-effect transistor (J109, Fairchild). The drain of the field-effect transistor is wired to the sample through the AFM base and the source is directly connected to the AFM tip. A platinum-coated AFM cantilever (HQ:NSC15/Pt, MikroMasch) is used. In the peak force tapping (PFT) mode, the cantilever is not mechanically driven at its resonance. Instead, the sample stage is drive in the z-direction at a low frequency (typically 2 kHz), much below the cantilever resonant frequency, allowing for the distance between the tip and sample to change sinusoidally. At the upper turning point, the tip and sample are in contact for several tens of microseconds. The tip-sample interaction force, and thus the maximum cantilever deflection during contact, is controlled

by an external setpoint. A beam from a diode laser reflects off of the AFM cantilever and is detected by a quadrant photodiode sensor. The vertical deflection signals from the quadrant photodiode are sent to a data acquisition card (PXI-5122, National Instruments) at a sampling rate of 25 MHz to be digitized and subsequently processed by a computer with Labview (National Instruments).

A phase-lock loop is used to synchronize a TTL voltage waveform to the PFT frequency with an adjustable phase delay. The TTL voltage waveform is used to trigger a function generator (2022B, Hantek). When triggered, the function generator outputs square-wave pulses (between -5 V and 0 V) to the gate of the depletion-type FET (J109, Fairchild). The phase of the TTL waveform is adjusted to ensure that the FET switching occurs when the tip is still very close to the sample (< 5 nm), so that the induced oscillation is strong. Multiple pulses are used, with a period between the pulses set to match the cantilever free-space oscillation period, in order to increase the SNR. During each pulse, the FET is in the ON state, and charges are free to flow between tip and sample. When the FET is in the OFF state, its residual capactances acts as a capacitor and draw charges from the tip and sample, removing Coulomb forces. The duty cycle within the square wave pulses are set to be 50%, so that the appearance and disspearance of the Coulomb force are exactly out of phase with respect to the cantilever oscillation, leading to an overall increase of the cantilever oscillation amplitude. Supplementary Figure S3 schematically describes the operation mechanism. Due to the high Q-factor of the tip (HQ:NSC15, Pt coated, Mikromasch), the induced oscillations persist until the next tip-sample contact, unless neutralized with the negative feedback loop. Resistors are included to mediate the flow of electrons and ensure fast switching of the ON/OFF states of the FET.

After digitization, the vertical deflection signals that correspond to the induced oscillations are converted to the frequency domain through a fast-Fourier transform. A single resulting peak at the cantilever resonance is extracted, integrated, and used as the real-time process variable for the negative feedback loop. The negative feedback loop from HF2Li-PID (Zurich Instruments) controls a DC voltage between tip and sample which maintains the tip oscillation at an external setpoint. To obtain the true CPD, the value from the non-zero setpoint is offset using the slope of the oscillation amplitude $vs.\ V_{DC}$ relation, as shown in **Figure 4.** The typical line scan speed for PF-KPFM is 0.2 Hz, resulting in image acquisition times of around 20 minutes per frame.

The Supporting Information is available free of charge at

• Cantilever deflection curves acquired at setpoints close to π, 0, and π/2, comparative surface potential images acquired with PF-KPFM and FM-KPFM, spatial resolution measurement for FM-KPFM, comparative amplitude error images acquired with PF-KPFM and FM-KPFM, comparison of lateral amplitude error width between PF-KPFM and FM-KPFM, schematic of charge migration during FET ON/OFF states.

Acknowledgments

We cordially thank the help from Wenpeng Cao for the preparation of the protein sample. D. S. J., H. W. and X. G. X. would like to thank the support from National Science Foundation CHE 1847765. X. G. X. would like to thank the Arnold and Mabel Beckman Foundation for the Beckman Young Investigator Award.

Author Contributions

X.G.X. designed the method. D.S.J. built the experimental apparatus. D.S.J carried out the experiment, the collection, and analysis of data. H. W. provided the protein sample and assistance on the signal acquisition. D.S.J. and X.G.X. participated in writing the manuscript. X.G.X. guided the overall research.

Conflict of Interest

We declare no conflict of interest.

References

- 1. Kelvin, L., V. Contact Electricity of Metals. *Philos. Mag.* **1898**, 46, 82-120.
- 2. Melitz, W.; Shen, J.; Kummel, A. C.; Lee, S., Kelvin Probe Force Microscopy and Its Application. *Surf. Sci. Rep.* **2011**, *66*, 1-27.
- 3. Kahn, A., Fermi Level, Work Function and Vacuum Level. Mater. Horiz. 2016, 3, 7-10.
- 4. Leung, T.; Kao, C.; Su, W.; Feng, Y.; Chan, C., Relationship between Surface Dipole, Work Function and Charge Transfer: Some Exceptions to an Established Rule. *Phys. Rev. B* **2003**, *68*, 195408.
- 5. Mönch, W., Metal-Semiconductor Contacts: Electronic Properties. Surf. Sci. 1994, 299, 928-944.
- 6. Lim, S.; Elim, H.; Gao, X.; Wee, A.; Ji, W.; Lee, J.; Lin, J., Electronic and Optical Properties of Nitrogen-Doped Multiwalled Carbon Nanotubes. *Phys. Rev. B* **2006**, *73*, 045402.
- 7. Sohn, A.; Kim, H.; Kim, D.-W.; Ko, C.; Ramanathan, S.; Park, J.; Seo, G.; Kim, B.-J.; Shin, J.-H.; Kim, H.-T., Evolution of Local Work Function in Epitaxial VO₂ Thin Films Spanning the Metal-Insulator Transition. *Appl. Phys. Lett.* **2012**, *101*, 191605.
- 8. Kikukawa, A.; Hosaka, S.; Imura, R., Silicon *PN* Junction Imaging and Characterizations Using Sensitivity Enhanced Kelvin Probe Force Microscopy. *Appl. Phys. Lett.* **1995**, *66*, 3510-3512.
- 9. Shvebelman, M. M.; Agronin, A. G.; Urenski, R. P.; Rosenwaks, Y.; Rosenman, G. I., Kelvin Probe Force Microscopy of Periodic Ferroelectric Domain Structure in KTiOPO₄ Crystals. *Nano Lett.* **2002**, *2*, 455-458.
- 10. Xiao, Z.; Yuan, Y.; Shao, Y.; Wang, Q.; Dong, Q.; Bi, C.; Sharma, P.; Gruverman, A.; Huang, J., Giant Switchable Photovoltaic Effect in Organometal Trihalide Perovskite Devices. *Nat. Mater.* **2015**, *14*, 193.
- 11. Ravi, S. K.; Rawding, P.; Elshahawy, A. M.; Huang, K.; Sun, W.; Zhao, F.; Wang, J.; Jones, M. R.; Tan, S. C., Photosynthetic Apparatus of Rhodobacter Sphaeroides Exhibits Prolonged Charge Storage. *Nat. Commun.* **2019**, *10*, 902.
- 12. Liscio, A.; Palermo, V.; Gentilini, D.; Nolde, F.; Müllen, K.; Samorì, P., Quantitative Measurement of the Local Surface Potential of π -Conjugated Nanostructures: A Kelvin Probe Force Microscopy Study. *Adv. Funct. Mater.* **2006**, *16*, 1407-1416.
- 13. Nonnenmacher, M.; O'Boyle, M.; Wickramasinghe, H. K., Kelvin Probe Force Microscopy. *Appl. Phys. Lett.* **1991**, *58*, 2921-2923.
- 14. Kitamura, S.; Iwatsuki, M., High-Resolution Imaging of Contact Potential Difference with Ultrahigh Vacuum Noncontact Atomic Force Microscope. *Appl. Phys. Lett.* **1998**, *72*, 3154-3156.
- 15. Ma, Z. M.; Kou, L.; Naitoh, Y.; Li, Y. J.; Sugawara, Y., The Stray Capacitance Effect in Kelvin Probe Force Microscopy Using FM, AM and Heterodyne AM Modes. *Nanotechnology* **2013**, *24*, 225701.
- 16. Colchero, J.; Gil, A.; Baró, A. M., Resolution Enhancement and Improved Data Interpretation In Electrostatic Force Microscopy. *Phys. Rev. B* **2001**, *64*, 245403.
- 17. Moores, B.; Hane, F.; Eng, L.; Leonenko, Z., Kelvin Probe Force Microscopy in Application to Biomolecular Films: Frequency Modulation, Amplitude Modulation, and Lift Mode. *Ultramicroscopy* **2010**, *110*, 708-711.
- 18. Giessibl, F. J., Advances in Atomic Force Microscopy. Rev. Mod. Phys. 2003, 75, 949.
- 19. Rosa-Zeiser, A.; Weilandt, E.; Hild, S.; Marti, O., The Simultaneous Measurement of Elastic, Electrostatic and Adhesive Properties by Scanning Force Microscopy: Pulsed-Force Mode Operation. *Meas. Sci. Technol.* **1997**, *8*, 1333.
- 20. Pittenger, B.; Erina, N.; Su, C., Quantitative Mechanical Property Mapping at the Nanoscale With Peakforce QNM. *Appl. Note Veeco Instrum. Inc.* **2010**, 1-12.
- 21. Lide, D. R., CRC Handbook of Chemistry and Physics 89 ed.; CRC Press: Boca Raton, Florida, 2008; p 12–114.
- 22. Garrett, J. L.; Munday, J. N., Fast, High-Resolution Surface Potential Measurements in Air with Heterodyne Kelvin Probe Force Microscopy. *Nanotechnology* **2016**, *27*, 245705.
- 23. Novikov, A., Experimental Measurement of Work Function in Doped Silicon Surfaces. *Solid-State Electron.* **2010**, *54*, 8-13.

- 24. Wang, L.; Wagner, M.; Wang, H.; Pau-Sanchez, S.; Li, J.; Edgar, J. H.; Xu, X. G., Revealing Phonon Polaritons in Hexagonal Boron Nitride by Multipulse Peak Force Infrared Microscopy. *Adv. Opt. Mater.* **2019**, 1901084.
- 25. Chen, X.; Yamada, H.; Horiuchi, T.; Matsushige, K.; Watanabe, S.; Kawai, M.; Weiss, P., Surface Potential of Ferroelectric Thin Films Investigated by Scanning Probe Microscopy. *J. Vac. Sci. Technol. B* **1999,** *17*, 1930-1934.
- 26. Trolier-McKinstry, S.; Muralt, P., Thin Film Piezoelectrics for MEMS. *J. Electroceram.* **2004**, *12*, 7-17.
- 27. Aksel, E.; Jones, J. L., Advances in Lead-Free Piezoelectric Materials for Sensors and Actuators. *Sensors* **2010**, *10*, 1935-1954.
- 28. Gallego-Juarez, J., Piezoelectric Ceramics and Ultrasonic Transducers. J. Phys. E: Sci. Instrum. 1989, 22, 804.
- 29. Tang, P.; Towner, D.; Hamano, T.; Meier, A.; Wessels, B. W., Electrooptic Modulation up to 40 GHz in a Barium Titanate Thin Film Waveguide Modulator. *Opt. Express* **2004**, *12*, 5962-5967.
- 30. Huang, H., Solar Energy: Ferroelectric Photovoltaics. Nat. Photonics 2010, 4, 134.
- 31. Uchino, K., Ferroelectric Devices. CRC Press: Boca Raton, Florida, 2018; p 235.
- 32. Kalinin, S. V.; Morozovska, A. N.; Chen, L. Q.; Rodriguez, B. J., Local Polarization Dynamics in Ferroelectric Materials. *Rep. Prog. Phys.* **2010**, *73*, 056502.
- 33. Döring, J.; Lang, D.; Wehmeier, L.; Kuschewski, F.; Nörenberg, T.; Kehr, S. C.; Eng, L. M., Low-Temperature Nanospectroscopy of the Structural Ferroelectric Phases in Single-Crystalline Barium Titanate. *Nanoscale* **2018**, *10*, 18074-18079.
- 34. Leung, C.; Kinns, H.; Hoogenboom, B. W.; Howorka, S.; Mesquida, P., Imaging Surface Charges of Individual Biomolecules. *Nano Lett.* **2009**, *9*, 2769-2773.
- 35. Sinensky, A. K.; Belcher, A. M., Label-Free and High-Resolution Protein/DNA Nanoarray Analysis Using Kelvin Probe Force Microscopy. *Nat. Nanotechnol.* **2007**, *2*, 653.
- 36. Gao, P.; Cai, Y., Label-Free Detection of the Aptamer Binding on Protein Patterns Using Kelvin Probe Force Microscopy (KPFM). *Anal. Bioanal. Chem.* **2009**, *394*, 207-214.
- 37. Navarra, G.; Peres, C.; Contardi, M.; Picone, P.; San Biagio, P. L.; Di Carlo, M.; Giacomazza, D.; Militello, V., Heat-and pH-Induced BSA Conformational Changes, Hydrogel Formation and Application as 3D Cell Scaffold. *Arch. Biochem. Biophys.* **2016**, *606*, 134-142.
- 38. Leng, Y.; Williams, C.; Su, L.; Stringfellow, G., Atomic Ordering of GaInP Studied by Kelvin Probe Force Microscopy. *Appl. Phys. Lett.* **1995**, *66*, 1264-1266.
- 39. Ding, J.; Strelcov, E.; Kalinin, S. V.; Bassiri-Gharb, N., Spatially Resolved Probing of Electrochemical Reactions *via* Energy Discovery Platforms. *Nano Lett.* **2015**, *15*, 3669-3676.
- 40. Strelcov, E.; Jesse, S.; Huang, Y.-L.; Teng, Y.-C.; Kravchenko, I. I.; Chu, Y.-H.; Kalinin, S. V., Space-and Time-Resolved Mapping of Ionic Dynamic and Electroresistive Phenomena in Lateral Devices. *ACS Nano* **2013**, *7*, 6806-6815.
- 41. Wang, L.; Wang, H.; Wagner, M.; Yan, Y.; Jakob, D. S.; Xu, X. G., Nanoscale Simultaneous Chemical and Mechanical Imaging *via* Peak Force Infrared Microscopy. *Sci. Adv.* **2017**, *3*, e1700255.
- 42. Wang, H.; Wang, L.; Jakob, D. S.; Xu, X. G., Tomographic and Multimodal Scattering-Type Scanning Near-Field Optical Microscopy with Peak Force Tapping Mode. *Nat. Commun.* **2018**, *9*, 2005.

Figures

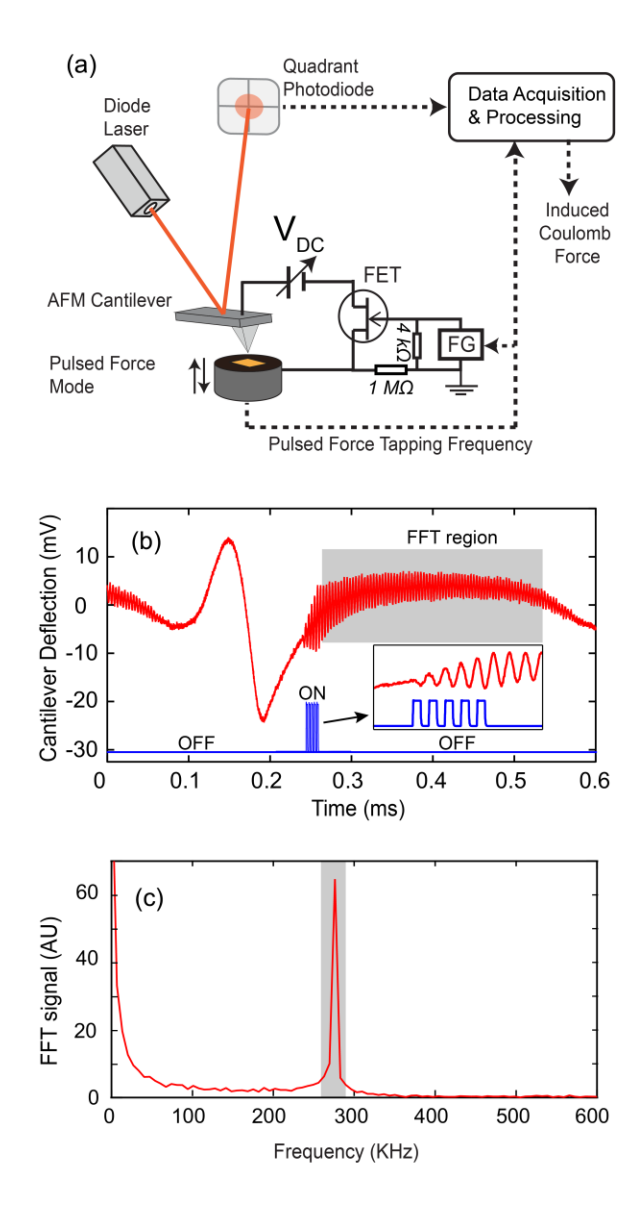


Figure 1. The signal collection mechanism of PF-KPFM. **(a)** Experimental setup. **(b)** The cantilever deflection trace (red) showing the mechanical oscillations induced by Coulomb force between tip and the sample. The voltage pulse train (blue) shows the moments at which electrical connections are switched ON. The oscillations of the cantilever deflection is digitized and are processed with FFT (shaded area). The voltage pulse train and induced mechanical oscillations are shown in greater detail in the inset. **(c)** The signals in frequency domain from the Fourier transform across cantilever free-space resonant frequency are integrated and used as signal to represent the Coulomb force.

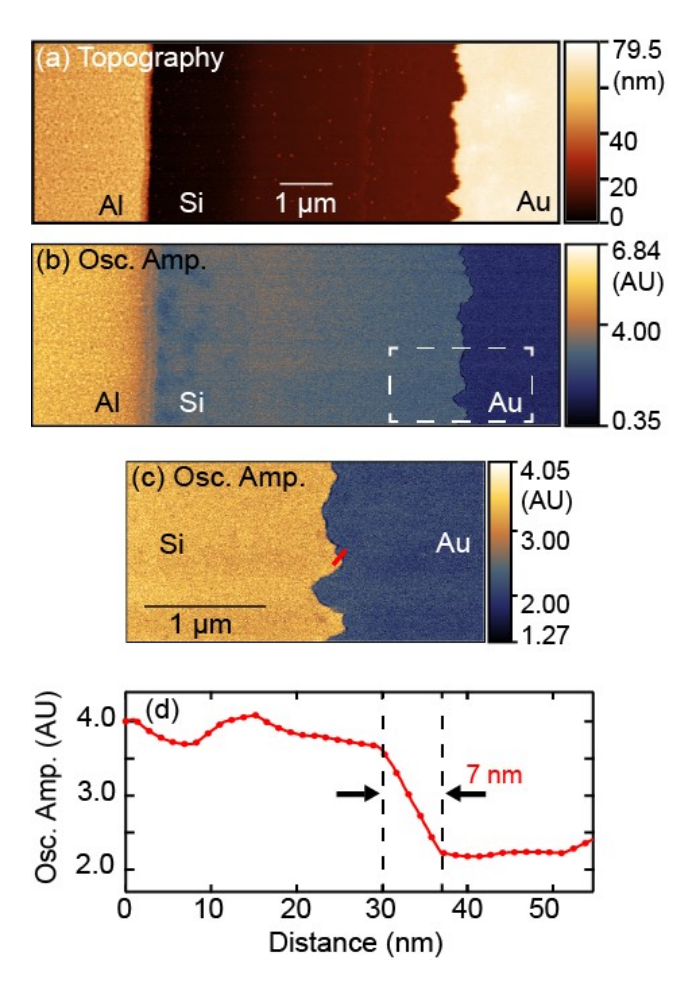


Figure 2. Spatial mapping of induced cantilever oscillations on an Al/Si/Au sample (a) The topography of the sample. The Al region is on the left; the Si region is in the middle; the Au region on the right. (b) The induced cantilever oscillation amplitude map across three regions. (c) The induced cantilever oscillation amplitude map between Si/Au region from the white dashed box marked in (b). (d) The spatial contrast is estimated from the small cross section marked by the red line (c). The spatial resolution of the induced Coulomb force measurement is determined to be 7 nm.

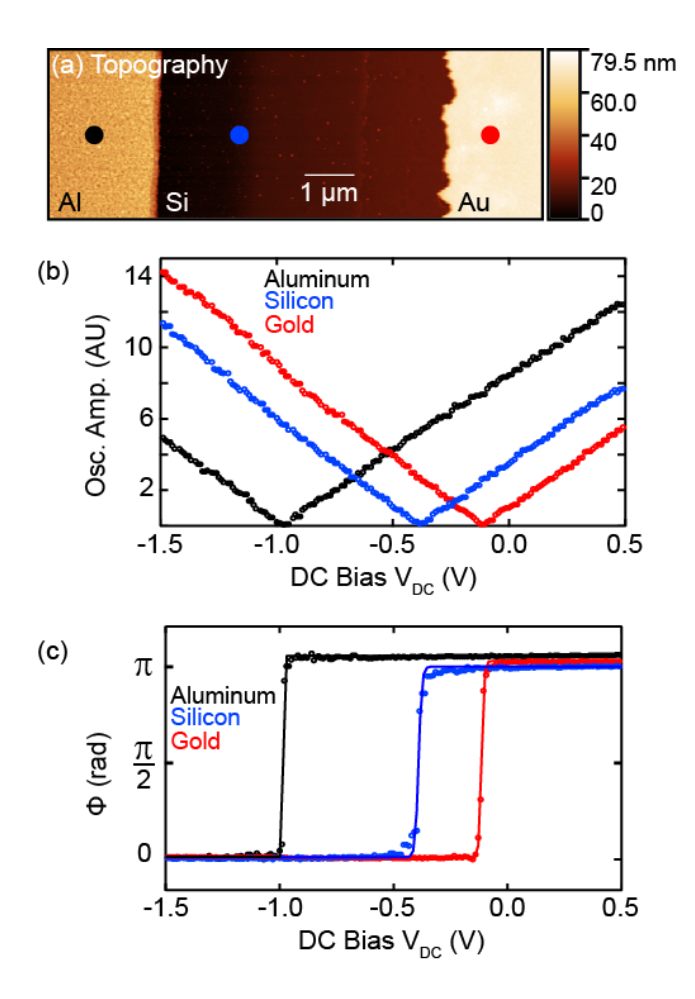


Figure 3. Measurement of CPD through sweeping V_{DC} . (a) Topography of the Al/Si/Au calibration sample. (b) The cantilever oscillations by induced Coulomb forces of the AFM tip while sweeping V_{DC} . The tip remains stationary over each metal in the locations marked by the colored circles in (a). The DC bias voltage in which the Kelvin force is neutralized is the CPD value. The measurement locations are marked by the colored circles in (a). (c) The phase of the cantilever oscillation *versus* applied DC bias V_{DC} . The CPD is found as the DC offset which results in an oscillation phase of $\pi/2$.

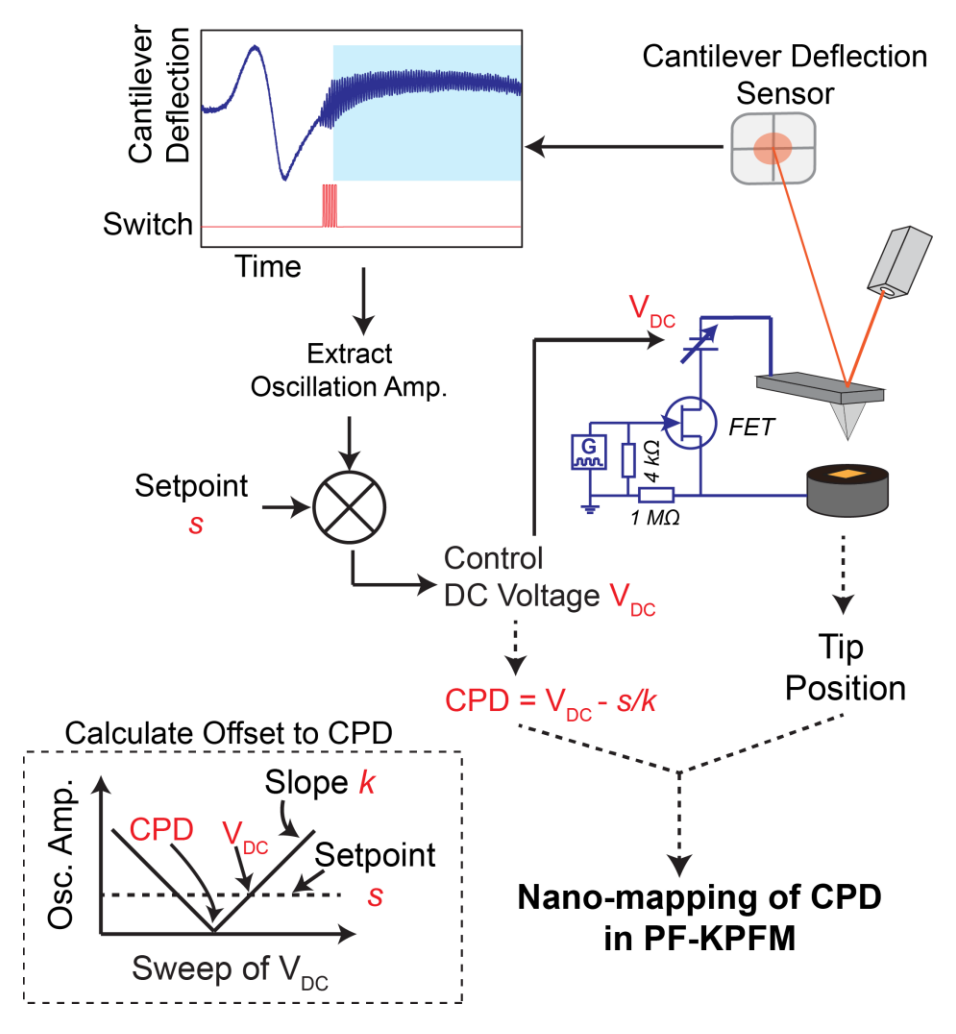


Figure 4. Schematics of the closed-loop CPD-mode of the PF-KPFM. The inset within the dashed box shows the derivation of the slope k.

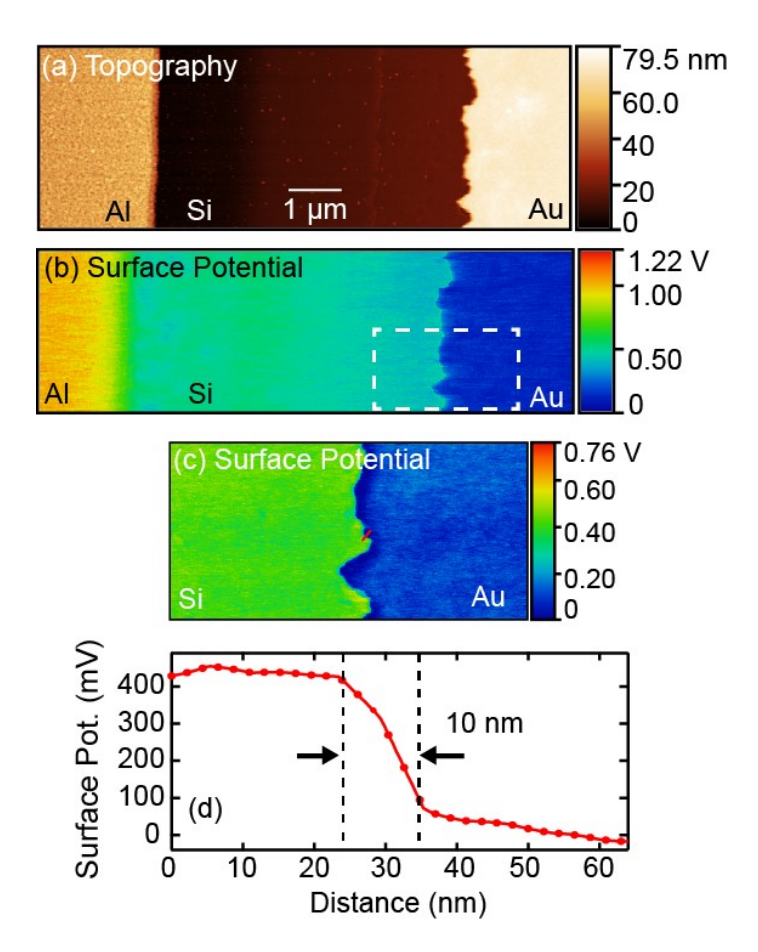


Figure 5. CPD mapping by PF-KPFM with feedback loop. **(a)** The topography of the Al/Si/Au calibration sample. **(b)** Surface potential measurement on the benchmark sample. The area is identical to that in Figure 2. **(c)** Surface potential measurement on a zoomed-in region shown by the white box in **(a)**. **(d)** The spatial resolution of PF-KPFM is shown to be 10 nm. The cross-section is extracted from the red line shown in **(c)**.

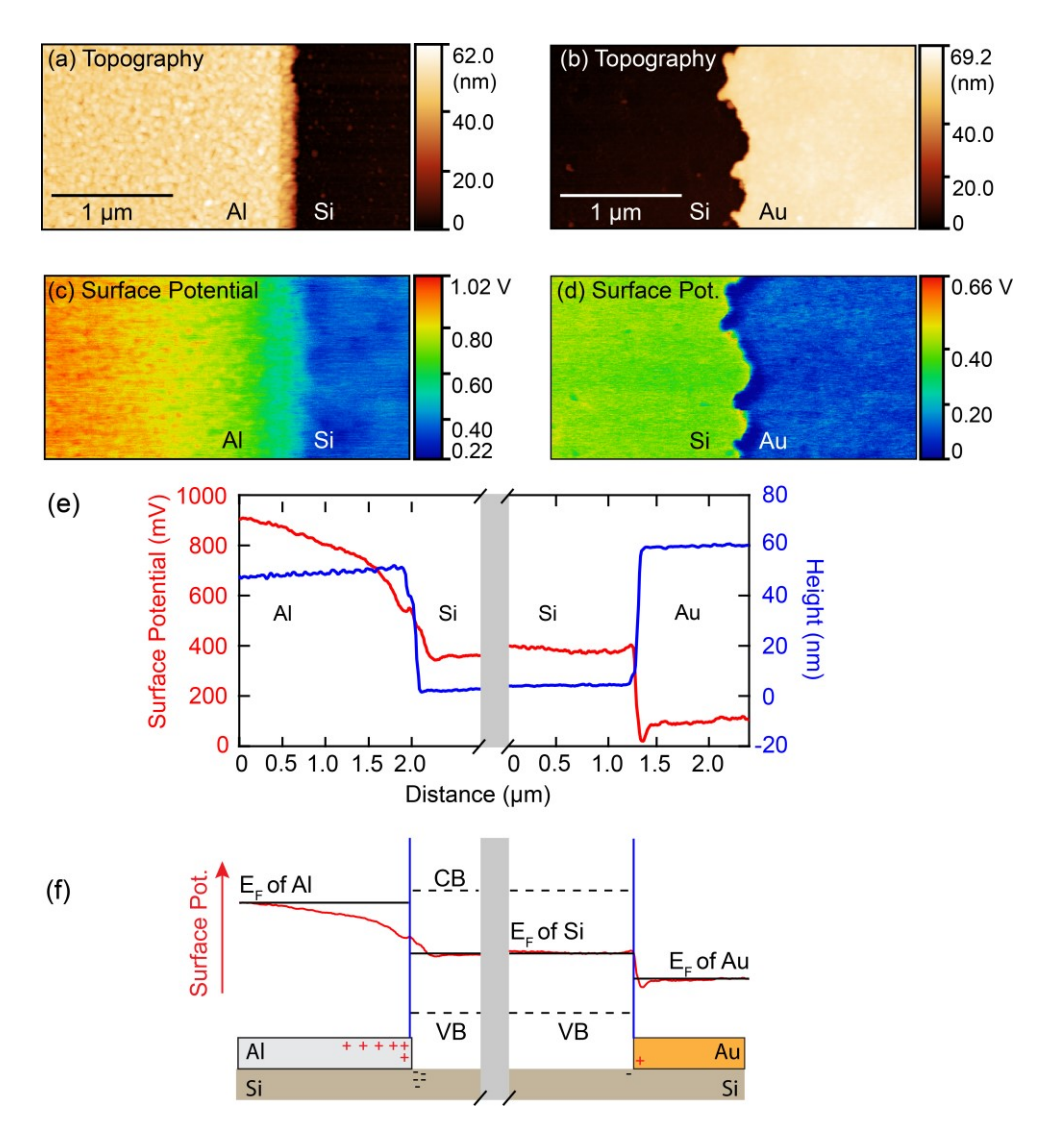


Figure 6. Bending of the surface potential between at boundaries. (a) Topography of an Al/Si boundary. (b) Surface potential map of the same region in (a). (c) Topography of a Si/Au boundary. (d) Surface potential map of the same region in (c). (e) Extracted profiles of surface potential values and topography across Al/Si and Si/Au boundaries. The spatial variation of the surface potential exhibits band bending behavior. Note that the measured surface potential values are inverse of the CPD between the sample and the platinum coated AFM probe. A larger value of surface potential in this measurement means a lower Fermi level. (f) Schematic illustration of the sample and its electrical properties. The relative position of each Fermi level prior to electrical contact is depicted. The surface potential of Al, *p*-doped Si, and Au, conduction band (CB) and valence band (VB) of Si, and the accumulation of charges as a result of contact are shown. The downward bending surface potential curve suggests accumulation of positive charges, and upward bending suggests accumulation of local electrons.

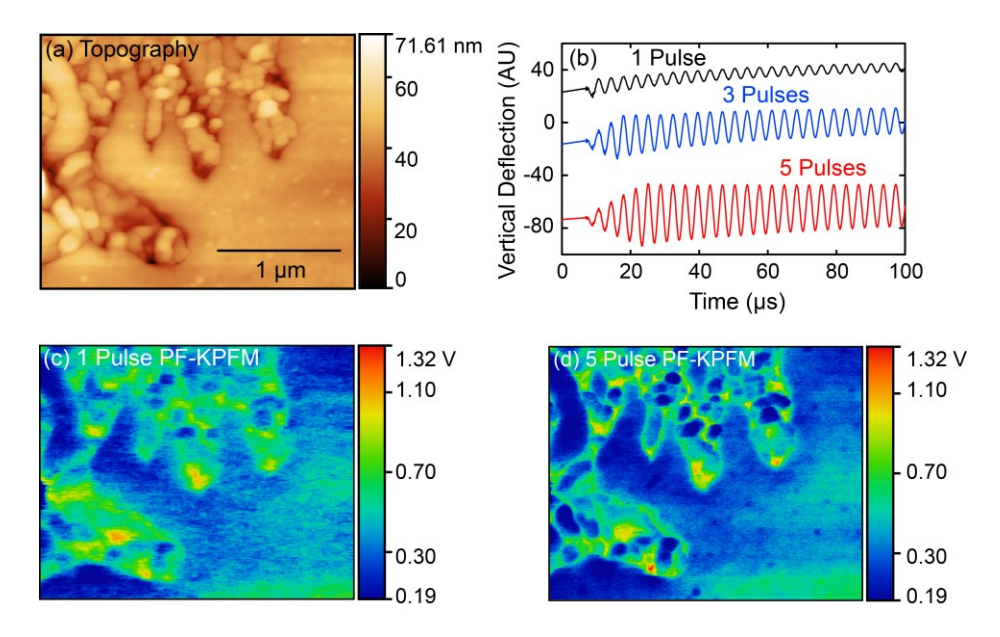


Figure 7. Improvement of the signal quality of PF-KPFM with multipulse FET switching. (a) Topography of a $MAPbBr_3$ perovskite sample. (b) Cantilever oscillations induced by 1-, 3-, and 5-pulse electrical connections. (c) The measured surface potential of the perovskite sample using the 1-pulse regime. (d) The same area measured by the 5-pulse regime. The scale bar is 1 μ m. Note that the increased signal to noise ratio from multi-pulse FET switching does not affect the values of the surface potential.

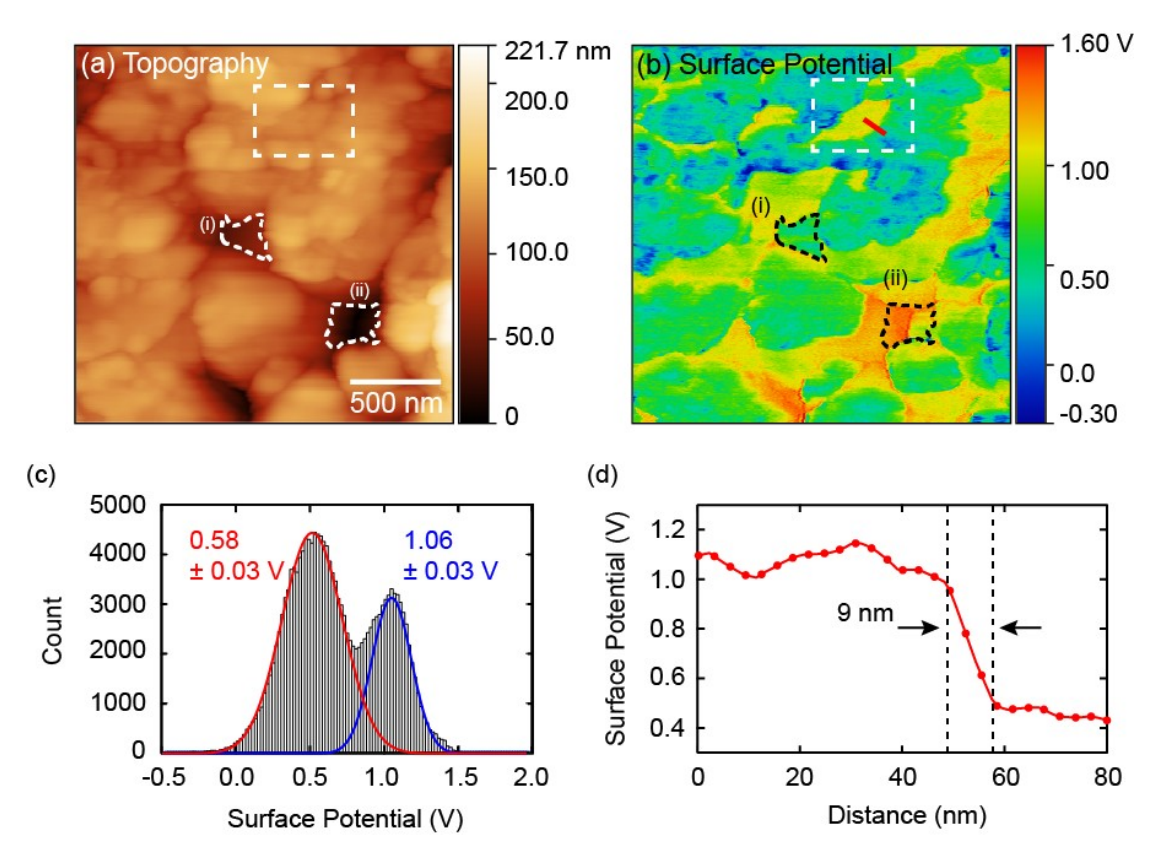


Figure 8. PF-KPFM measurement on compacted BaTiO₃ powders. (a) Topography of the BaTiO₃ surface. The scale bar is 500 nm. (b) Surface potential image of the BaTiO₃ surface. The dotted black lines marked 1 and 2 indicate two separate grains which show much different surface potential values despite both exhibiting low topography around adjacent grains. The white dotted box shows a grain that has a high surface potential surrounded by grains of much lower surface potential. (c) A histogram created from the surface potential data shows two prominent values, suggesting two primary unit cell elongation directions. (d) A spatial resolution of 9 nm for PF-KPFM is extracted from the red line in (b).

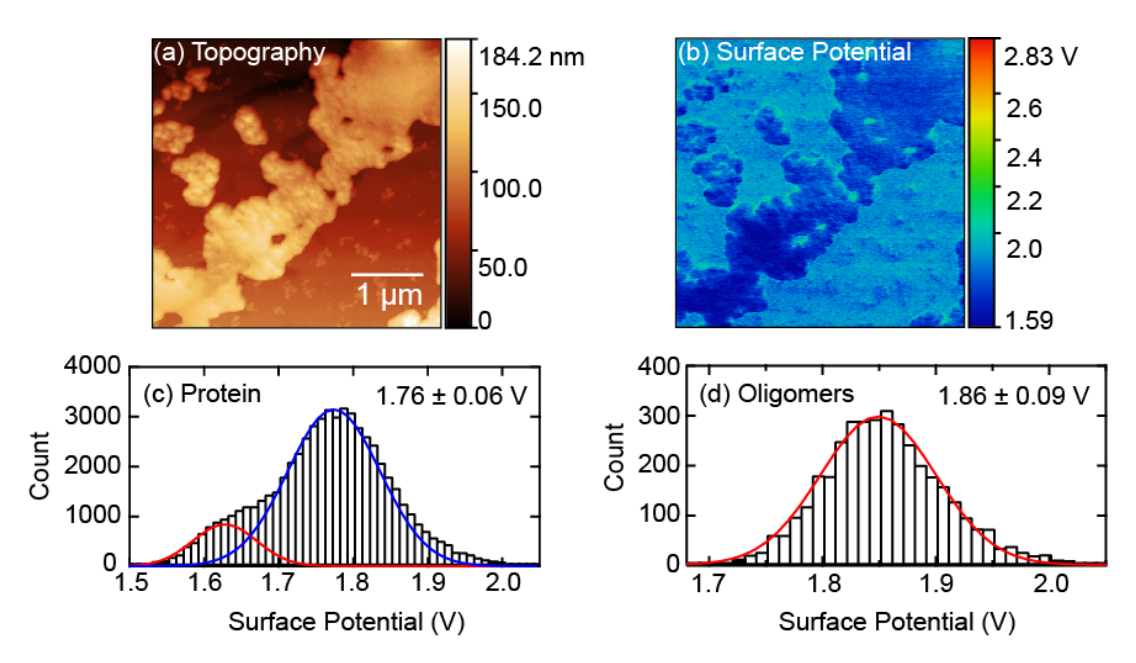


Figure 9. Multimodal PF-KPFM measurement on bovine serum albumin (BSA) protein deposited on a Si substrate. (a) Topography of the BSA structure. The protein structure is present together with oligomers on the surface of the substrate. (b) Surface potential mapping of the BSA protein and surrounding oligomers. (c) A background-subtracted histogram shows the surface potential range of the protein structure to show the heterogeneity of the surface potential. The average surface potential value for the protein is $1.76 \pm 0.06 \text{ V}$, taken as the average of the main peak. (d) A background-subtracted histogram shows the surface potential range for the oligomers only. The average surface potential value for the oligomers is $1.86 \pm 0.09 \text{ V}$.

For Table of Contents only

